



TECHNICAL ARTICLE

Microstructure and Properties of Pulse Tungsten Inert Gas Welded Joint for Different Thickness CR22MnB5/DH1050 Dissimilar High-Strength Steel

Hongju Fan, Peng Liu, Kang Xiao, Chengge Wu, Chuanwei Shi, and Yongbin Wang

Submitted: 23 May 2022 / Revised: 20 November 2022 / Accepted: 25 November 2022 / Published online: 8 December 2022

The CR22MnB5/DH1050 dissimilar high-strength steel in automotive crash beams was welded by the direct current pulse TIG welding method. The microstructure and mechanical properties of the joints under different post-weld tempering treatments were tested and analyzed. The present results had a certain effect on further improving the performance of high-strength welded joints to use in the auto structure. The result showed that the weld zone (WZ) of the as-weld joint basically consisted of lath martensite. With the increasing tempering temperature, the original lath martensite gradually transformed into tempered martensite and tempered sorbite, and the C-containing solid solution in α -Fe gradually decreases, increasing carbides and grain growth. The WZ had the highest hardness, and a soft zone existed in the heat-affected zone of all steels. After tempering treatments, the microhardness of welded joint decreased, and the hardness decreased obviously after tempering at 550 °C. After tempering at 250 °C, the tensile strength of the joint was reduced (about 7 MPa) compared with the base material (BM), and the elongation was increased by 0.27%. After tempering at 550 °C, the tensile strength of the joint decreased by 166 MPa compared with the BM, while the elongation increased by 4.8%. After tempering at 250 °C, the maximum bending load applied to the joint (516 N) decreased insignificantly compared to the as-weld joint (558 N), while the bending resistance of the specimen (438 N) decreased significantly after the high temperature at 550 °C. In addition, the electrochemical corrosion potential of the welded joint by tempering treatments was positively shifted and the corrosion resistance was improved.

Keywords dissimilar high-strength steel, mechanical properties, microstructure, P-TIG, tempering treatment

1. Introduction

At present, solving environmental problems has received worldwide attention. Some studies have concluded that 1/3 of greenhouse gas emissions originate from modern industry (Ref 1), among which carbon emissions caused by vehicle exhaust have a greater impact, and vehicle light-weighting is considered an effective strategy to solve this problem (Ref 2, 3). Some studies have shown that for every 10% reduction in vehicle weight, fuel consumption can be reduced by 6-8%. In recent years, there has been extensive research on lightweight alloy materials for automobiles, such as aluminum alloys, magnesium alloys and high-strength steels (Ref 4). However, the application of high-strength steels in automotive structures is still indispensable due to considerations of materials and their processing costs. The ideal automotive structure should have

the ability to absorb higher energy during a collision, which requires the development of advanced high-strength steels (AHSS) to support this strategic requirement (Ref 5-7). AHSS can replace low-carbon soft steels in the form of thinner parts and achieve weight reduction without sacrificing crash performance, so they are widely used in the manufacture of some automotive body-in-white components at the moment.

CR22MnB5 steel is an ultra-high-strength boron steel plate (Ref 8, 9), which is usually quenched and its strength can be substantially increased then assembled for welding. However, the heat-affected zone (HAZ) of the welded joint is prone to induce softening problems, and the mechanical properties of the joint are reduced. In addition, DH1050 high-strength steel is a modified dual-phase steel containing mainly martensite and ferrite (Ref 10, 11), and the presence of some residual austenite can improve plastic deformability and has a high elongation. Multiple DP grades can be produced by controlling the martensite volume fraction (MVF) (Ref 12). The current design of automotive structures often requires the use of lightweight sheet materials, such as the A, B and C pillars on the body of the car, front and rear bumpers, floor channels, door reinforcements and roof side beams. Most of the components are optimized for structural optimization using the tailor welded blanks (TWB) technology to reduce the mass of the whole welded plate, so as to reduce the body mass and fuel consumption (Ref 13, 14), while the process of thin plate welding is prone to serious welding deformation problem. Currently, the more widely used TWB techniques include laser welding (LW), resistance spot welding (RSW), friction stir

Hongju Fan, Peng Liu, Kang Xiao, Chuanwei Shi, and Yongbin Wang, School of Materials Science and Engineering, Shandong Jianzhu University, Jinan 250101, People's Republic of China; Chengge Wu, School of Construction Machinery, Shandong Jiaotong University, Jinan 250357, People's Republic of China. Contact e-mail: liupeng1286@163.com.

welding (FSW) and gas shielded welding (GSW) (Ref 15, 16). Zhang (Ref 17) et al. studied the microstructure and mechanical properties of 2.0-mm-thick DP780 sheet joints by varying the RSW parameters. When the welding current was 9.5 kA, the welding time was 400 ms. When the welding pressure was 5 kN, the joint had the maximum shear force and fusion nucleus diameter with good shear resistance. Under conditions of constant spot-welding time and pressure, the microhardness of the nucleus zone decreased with the increase in welding current. Hayat (Ref 18) and others studied the fracture toughness of lap RSW joint for galvanized DP600 steel and found that the toughness of the joint was related to the welding current, welding time and hardness. The toughness of the joint increased with the increase of welding current and welding time, but excessive welding current and welding time resulted in a decrease in toughness. Since high-strength steels contain more alloying elements compared to low-strength steels, they have a higher resistivity and the contact surface of the steel plate heats up quickly and is prone to spatter, so the problem of differences in properties between dissimilar unequal-thickness materials should be considered when designing the spot-welding process (Ref 19). Farabi (Ref 20) et al. studied the microstructure and mechanical properties of laser welded DP600 steel joint. Due to the rapid heating and cooling effect, the WZ shows martensitic structure and leads to a significant increase in its hardness, and a significant tempering softening zone in HAZ, while the tensile specimens of the joint fracture in HAZ show ductile fracture characteristics. The tensile strength of the joint remains almost unchanged compared to base metal (BM), and the joint obtains high yield strength. The LW has high energy density, fast welding process and low heat transfer, which can minimize the differences in the structure of various areas of the joint, reduce the thermal deformation of the workpiece and other problems. Therefore, it is very suitable for thin welding plates of automotive dissimilar high-strength steel. In comparison, tungsten arc welding (TIG) is also widely used in the field of automotive body welding due to its lower cost and excellent joint performance (Ref 21). In recent years, with the development of the pulse-type tungsten arc welding (P-TIG) method, high quality complex thin-walled unequal-thickness dissimilar high-strength steel stitching can be achieved (Ref 22-25). Rossini (Ref 15) et al. studied the welding process of high-strength heterogeneous TWIP/TRIP steels and their joint properties using the non-filtered TIG welding method. The results show that satisfactory heterogeneous joints can be obtained for heterogeneous high-strength steel TRIP/TRIP, and there is a relationship between the forming of the joint during welding and the gas flow rate. Although the TWIP/TWIP joints have good mechanical properties, in the absence of filler material TRIP/TWIP joints are poorly formed. Eszter (Ref 26) and others through the optimization of the welding process parameters, successfully obtained the TRIP800/TWIP1000 steel splice weld head, the tensile fracture of the joint presents significant ductile fracture characteristics, and the joint hardness distribution on the TRIP steel side is relatively good. However, so far, the research on TIG welding or P-TIG welding technology for dissimilar thin high-strength steel is still insufficient, and with the emergence of various new thin high-strength steel and its application diversification and complexity, it is necessary to carry out TIG welding technology and basic research on various new dissimilar steel.

In this paper, a new type of dissimilar ultra-high-strength steel CR22MnB5/DH1050 for automotive is used as the testing material, and the pre-weld heat treatment process of the welded plate is designed using the P-TIG process to determine the welding process parameters for processability test analysis. The microstructure, mechanical and corrosion properties of welded joints were studied. The influence mechanism of post-weld tempering treatment process on the evolution of microstructure and properties of dissimilar steel joints was analyzed and discussed, which provided an experimental and theoretical basis for the research on the TIG butt welding technology of dissimilar thin plate high-strength steel.

2. Experimental

2.1 Materials and Welding Technology

A new type of dissimilar high-strength steel CR22MnB5 (thickness of 1.2 mm) /DH1050 (thickness of 0.85 mm) for automobiles was used in this study, and the P-TIG welding process was adopted. The welding drawing can be seen in Fig. 1(a). CR22MnB5 steel, cold rolling hot forming steel plate, was produced by Shougang Group, China, and the materials were provided with annealing treatment and no hot forming process. The size of the test steel plate is $150 \times 100 \times 1.2$ mm. The chemical composition of CR22MnB5 steel is shown in Table 1. CR22MnB5 steel is composed of ferrite + pearlite structure before hot forming (see Fig. 1b). The obvious pearlite structure is distributed in the lamellar form on the ferrite matrix. Figure 2(a) shows the tensile stress-strain curve of CR22MnB5 steel, and the tensile strength $R_m = 500$ MPa, elongation $A = 20.5\%$ (see Table 2). DH1050 steel is also a high-strength steel sheet with continuous annealing treatment manufactured by Shougang Group, China. The size of the test steel plate is $150 \times 100 \times 0.85$ mm. The chemical composition of DH1050 steel is shown in Table 1. The DH1050 steel is composed of island martensite structure (see Fig. 1c) and uniformly distributed in the ferrite matrix. And some retained austenite is distributed at the junction of martensite and ferrite structure. The tensile stress-strain curve of the DH1050 high-strength steel sheet is shown in Fig. 2(b). The tensile strength is $R_m = 985$ MPa and elongation $A = 18.3\%$ (see Table 2).

Before welding, the CR22MnB5 steel plate was treated by a 950°C water-cooled quenching process (see in Fig. 3). In this test, in order to simulate the heating and quenching process in the hot forming process, it is necessary to ensure that the heated sheet metal quickly and vertically enters the water for quenching treatment during quenching, so as to reduce the possible wave deformation during water quenching. The surface of the material needs to be mechanically cleaned of rust and impurities before welding, and then, the welded parts were accurately positioned and reliably clamped to facilitate the assurance of welding accuracy. The welding fixture designed in this test is shown in Fig. 4. However, due to the different thicknesses of the two materials, it is necessary to use shims of different thicknesses to flatten the two steel plates and then use bolts to connect and clamp, which can effectively avoid the generation of welding deformation.

Due to the use of unequal thickness of dissimilar steel materials in this study, welding processability tests are required

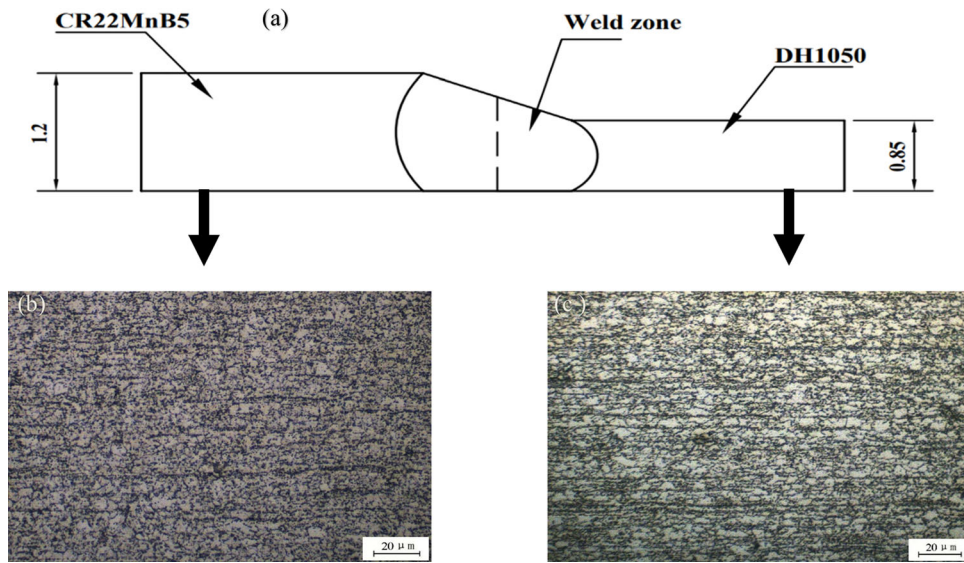


Fig. 1 Schematic diagram of the welding structure and microstructure of BM. (a) schematic diagram of the welding structure, (b) CR22MnB5 steel, (c) DH1050 steel

Table 1 The chemical composition of all test materials (Wt.%)

Materials	C	Si	Mn	P	S	Cr	Cu	d	Al	B	Ti
CR22MnB5	0.22	0.23	1.22	0.015	0.002	0.21	0.010	0.004	0.062	0.0028	0.042
DH1050	0.204	0.61	2.19	0.009	0.001	0.38	...	0.003	0.81	0.021	0.008

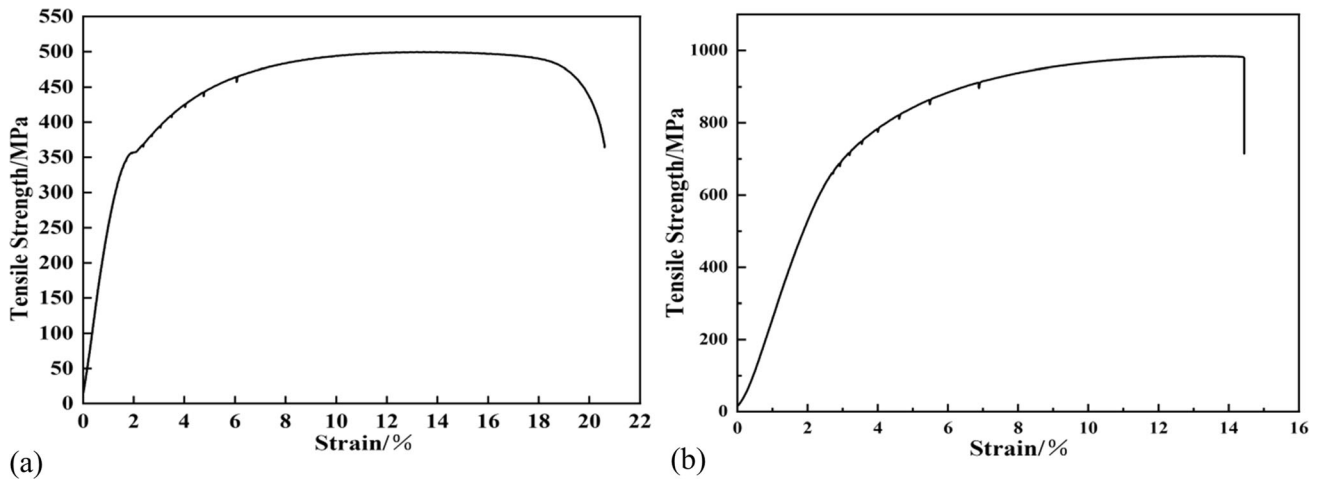


Fig. 2 The stress–strain curves of BM (a) CR22MnB5 steel, (b) DH1050 steel

Table 2 The tensile properties of base materials tested

Materials	Tensile strength, MPa	Yield strength, MPa	Elongation, %
CR22MnB5	500	457	20.5
DH1050	985	851	14.5

to determine the optimal welding process parameters. After a series of processability tests, the more appropriate welding process parameters are shown in Table 3. Under different

welding currents, CR22MnB5/DH1050 dissimilar high-strength steel was welded by P-TIG welding method, and the macroscopic morphology is shown in Fig. 5. When the welding

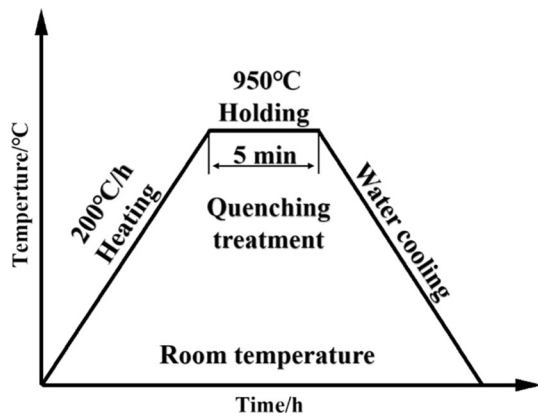


Fig. 3 The 950 °C water-cooled quenching process of CR22MnB5 steel before welding

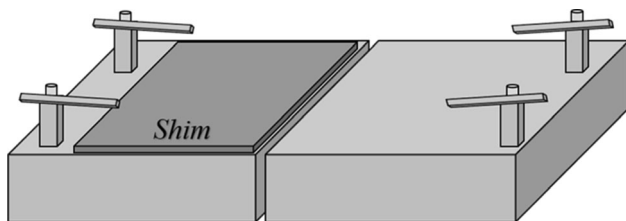


Fig. 4 The schematic of welding fixture to fix testing steel sheet

Table 3 The P-TIG welding process parameters for CR22MnB5/DH1050 dissimilar steel

Samples	Welding current, A	Welding speed, mm/s
1	60	3.42
2	70	3.42
3	80	3.42
4	90	3.42

current is $I = 80$ A, the joint shape is the best, and no obvious defects are observed (see Fig. 5e and f). When the welding current is $I = 60$ and 70 A (see Fig. 5a-d), the welded joint has obvious incomplete penetration. When the welding current $I = 90$ A (Fig. 5g), the typical weld-through phenomenon existed in the welded joint. Therefore, the optimum welding parameters are welding current $I = 80$ A and welding speed $V = 3.42$ mm/s.

In general, the uneven internal heating and the thermal expansion and the cold contraction of weld metal will cause residual stress during thin plate welding, which will lead to large welding deformation and non-uniformity of structure. Using tempering treatment can eliminate the residual stresses of welded joint, which helps to improve the plastic deformation capacity of the joint and prevent cracks produced after stamping of the tailor welded structure and lead to joint fracture. Table 4 shows the tempering process parameters of the welded joints used in this study, and the tempering heat treatment process curve is shown in Fig. 6.

2.2 Experiments and Characterization Methods

The metallographic samples of the welded joint (original and tempered) were cut by the lining cutting method, and corroded with 4% nitric acid + alcohol mixed solution. The microstructure, phase composition and element distribution of the joint were observed and analyzed by optical microscope (OM), Zeiss surtm55 thermal field emission scanning electron microscope (SEM) and EDS. DHV-1000 microhardness tester was used to test the microhardness distribution in each area of the joints with a loading load of 0.5 kg and a loading time of 10 s. The tensile strength of the joints was tested according to the standard GB/T228-2010 (China), the specimen size and sampling position were shown in Fig. 7. Three tensile specimens were prepared for testing under each parameter. Then WDW-100 electronic universal testing machine was used, and the tensile loading speed was 1 mm/min. The tensile strength calculation formula (1) and the elongation calculation formula (2) are as follows:

$$\sigma = \frac{F_b}{S_0} \quad (\text{Eq 1})$$

where σ is the tensile strength of the tensile specimen, MPa. F_b is the maximum load to which the specimen is subjected, N . S_0 is the original cross-sectional area at the parallel length of the specimen, mm^2 .

$$A = \frac{L_u - L_0}{L_0} \times 100\% \quad (\text{Eq 2})$$

where A is the elongation after break, %. L_0 is the original pitch of the tensile specimen, mm. L_u is the post-break distance of the tensile specimen, mm.

The joint bending test was prepared according to the standard GB/T232-2010(China). The shape, position and size of the test sample are shown in Fig. 8. The CM504 electronic universal testing machine is used for a three-point bending test. The back of the weld is mainly subjected to tensile stress, so the bending test is carried out with the back of the weld facing down, and the displacement speed of the indenter is 2 mm/min. Three groups of specimens for a bending test were prepared under each parameter. The calculation formula of span L in the three-point bending test is shown as (3). The span L is calculated to be 22 mm.

$$L = (d + 3a) \pm 0.5a \quad (\text{Eq 3})$$

where L is the span distance, mm; a is bending sample thickness, mm; d is bending indenter diameter, mm.

The CH660D electrochemical workstation was used for the electrochemical corrosion test, and a three-electrode system was adopted, that is, the working electrode was the joint (effective area 1cm^2), the auxiliary electrode was the platinum electrode, and the reference electrode is a saturated calomel electrode. Due to the HAZ is too narrow, the electrochemical corrosion specimens only were cut from WZ and BM of the joint by lining cutting in this study, with a specimen surface area of 10×10 mm, then the specimens were wax sealed. The experimental temperature was 25 °C, the corrosion medium was 3.5% NaCl solution, the potential range was ± 200 mV relative to the open circuit potential (OCP), and the scanning speed was 1 mV/s.

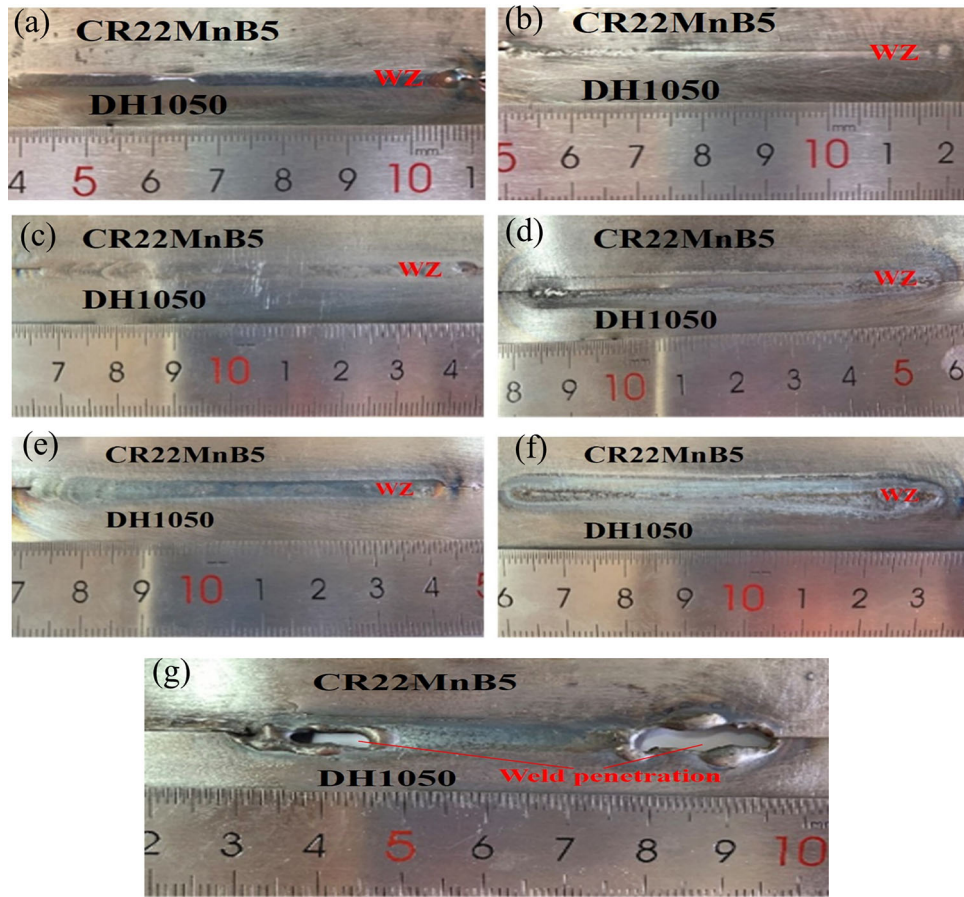


Fig. 5 The macro-morphology of CR22MnB5/DH1050 dissimilar steel joint under different welding currents. (a) Front side ($I = 60$ A, $V = 3.42$ mm/s), (b) Back side ($I = 60$ A, $V = 3.42$ mm/s), (c) Front side ($I = 70$ A, $V = 3.42$ mm/s), (d) Back side ($I = 70$ A, $V = 3.42$ mm/s), (e) Front side ($I = 80$ A, $V = 3.42$ mm/s), (f) Back side ($I = 80$ A, $V = 3.42$ mm/s), (g) Front side ($I = 90$ A, $V = 3.42$ mm/s)

Table 4 The heat treatment process of tempering for the welded joints

Sample	Temper temperature, °C	Holding time, h	Cooling method
1	Original state	Original state	Original state
2	250	1	Air cooling
3	550	1	Air cooling

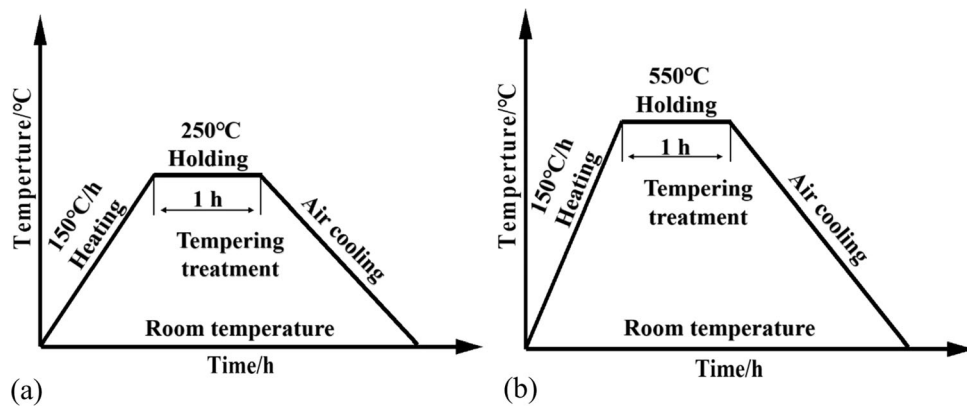


Fig. 6 The curve of tempering heat treatment for CR22MnB5/DH1050 welded joints (a) Tempering at 250 °C, (b) Tempering at 550 °C

3. Results and Discussion

3.1 Effect of Post-weld Heat Treatment on the Microstructure of the Joint

3.1.1 OM Analysis of the CR22MnB5 Side in HAZ. The macro-morphology of various regions for CR22MnB5/DH1050 dissimilar high-strength steel welded joints is shown in Fig. 9. Figure 10 shows the microstructure of CR22MnB5 side in HAZ under different tempering temperatures. The complete quenching zone of HAZ (see Fig. 10a) is a typical coarse lath martensite and retained austenite, which is due to the possible recrystallization of the zone near the weld center during reheating, resulting in grain coarsening (Ref 27).

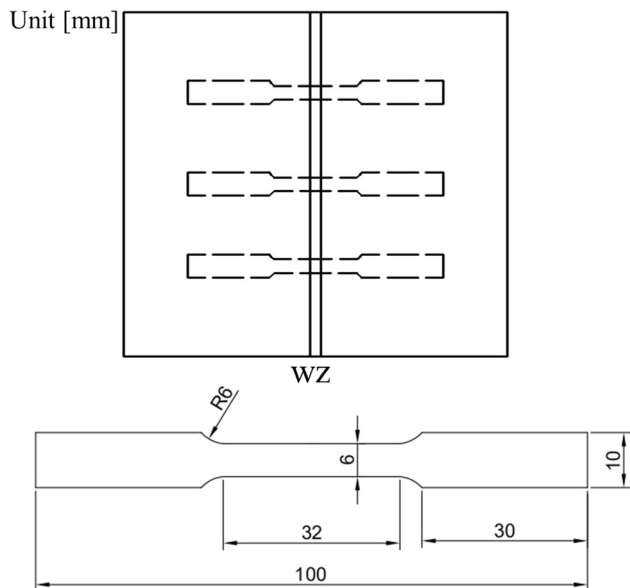


Fig. 7 The cutting position and size of samples for tensile testing

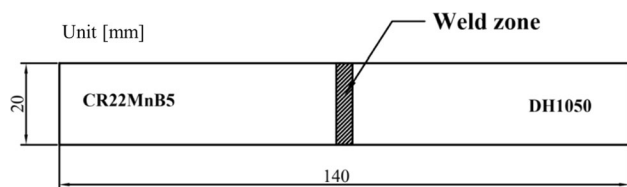


Fig. 8 The size of bending testing specimens for the CR22MnB5/DH1050 welded joint

The microstructure of the incomplete quenching zone near the BM side is shown in Fig. 10(b). The pearlite and partial ferrite in the original structure could experience the austenite transformation, and transform into lath martensite, ferrite and part of bainite after cooling. It is the fact that the region is far from the center of the heat source and the heat is not sufficient to transform all the original structure to martensite. This observation is consistent with that of Li (Ref 28), and it was found that this situation led to the formation of various phases below the temperature A_{c1} , including bainite and ferrite.

The microstructure in the complete quenching zone (see Fig. 10c) is mainly martensite and bainite after tempering at 250 °C compared with the original structure. Under the influence of low-temperature tempering, the martensite structure is further decomposed to form tempered martensite, and some retained austenite is decomposed and transformed into lower bainite. The microstructure of the incompletely quenching zone (see Fig. 10d) is slightly different from that of the no tempering zone. Some of the martensite structure is decomposed, the ferrite structure is increased, the grain becomes fine, and the cementite precipitates on the original austenite grain boundary and martensite interface to form a thin shell. In addition, there is a small amount of lower bainite structure, and its grains have grown compared with the original structure.

Compared with 250 °C tempering treatment, after 550 °C tempering treatment, the martensite structure in the complete quenching zone (see Fig. 10e) decomposes greatly and the bainite structure disappears under the action of high temperature. In the ferrite matrix formed during the tempering of martensite, there is a multiphase structure of fine spherical carbides (including cementite), i.e., tempered sorbite. At this time, there are still some lath martensite structures that have not been decomposed. The amount of ferrite in the incomplete quenching zone (see Fig. 10f) increases and the grain size increases. At this time, the martensite structure almost disappears, most of the structure is transformed into tempered sorbite with a small amount of retained austenite. The number of carbides increases significantly, the grain size increases, the shape becomes spherical and nearly spherical, and the distribution is relatively uniform.

3.1.2 OM Analysis of the Joint in WZ. Figure 11 shows the microstructure of WZ under different tempering treatments. The microstructure of the weld area of the original joint is shown in Fig. 11(a). Due to the highest heat input in the center of the weld, the ferrite and pearlite can be prompted to austenitization completely, while the rapid cooling rate prompts the formation of plate-like martensite that is elongated at an angle the heat dissipation direction after cooling, with uniform distribution (Ref 29). The presence of residual austenite structure can be seen at this point. In fact, in a study by Son

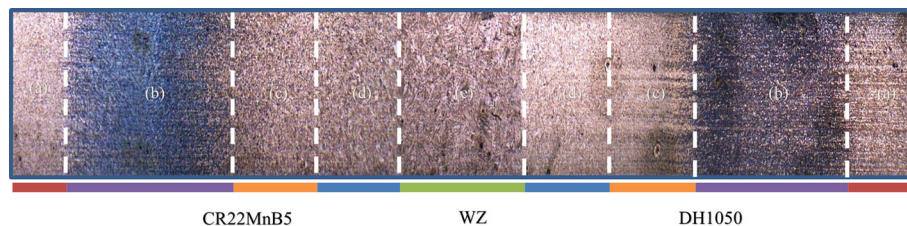


Fig. 9 The microstructure of all regions for the CR22MnB5/DH1050 welded joint. (a) Base metal, (b) incomplete quenching zone, (c) complete quenching zone (fine grain zone), (d) complete quenching zone (coarse grain zone), (e) weld zone

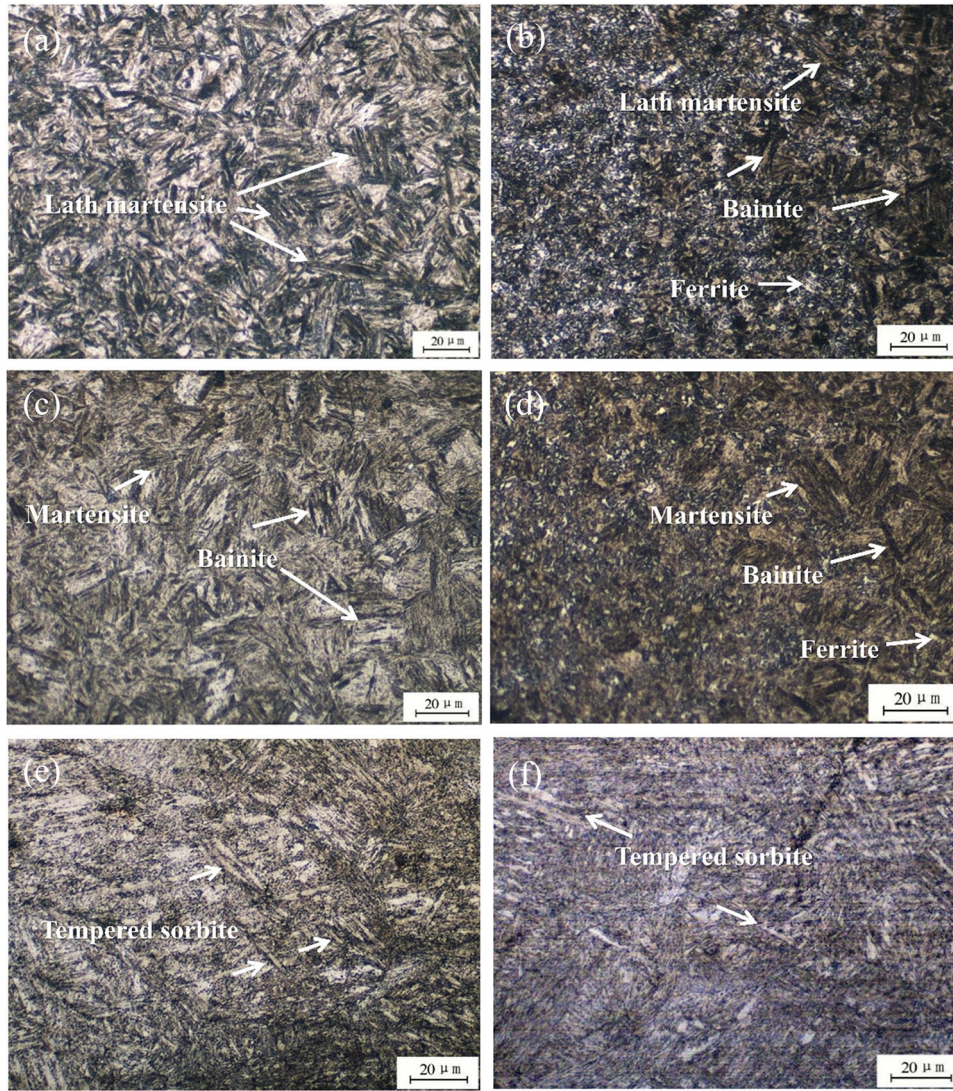


Fig. 10 The microstructure of HAZ on the CR22MnB5 side of the joint under different tempering treatments. (a) Complete quenching zone (no tempering), (b) incomplete quenching zone (no tempering), (c) complete quenching zone (tempering at 250 °C), (d) incomplete quenching zone (tempering at 250 °C), (e) complete quenching zone (tempering at 550 °C), (f) incomplete quenching zone (tempering at 550 °C)

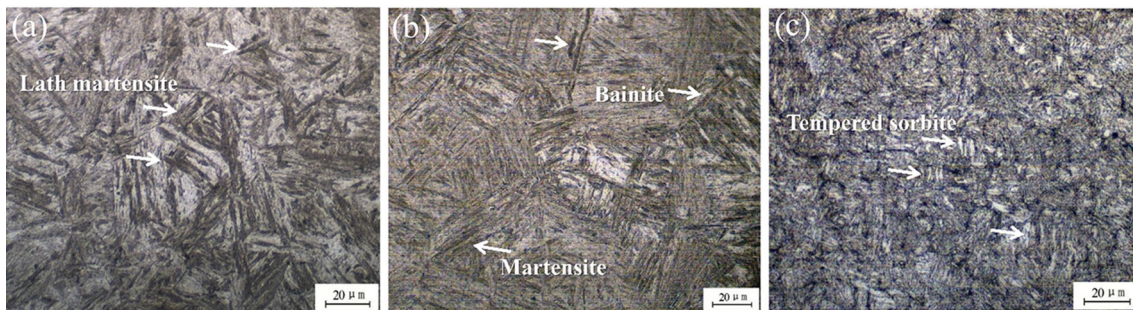


Fig. 11 The microstructure of WZ under different tempering treatments. (a) No tempering, (b) tempering at 250 °C, (c) tempering at 550 °C

(Ref 30) et al., it was found that the constituent phases in HAZ and WZ of the post-welded specimens consisted mainly of martensite and bainite. Figure 11(b) shows the microstructure of WZ after tempering treatment at 250 °C. It can be observed that the martensitic structure decomposes and transforms into

the tempered martensitic structure. With the residual austenite decomposition, and part of the structure transforms into lower bainite. The ferrite structure is slightly reduced and the grain size is smaller than the original structure. At this time, some solid-solution C atoms are precipitated directly in the form of

cementite, which are mainly located at the original austenite grain boundary, lath bundle boundary and lath block boundary. When tempering at 550 °C, the WZ structure (see Fig. 11c) decomposes greatly, the ferrite structure increases, and the precipitated particles are small spherical carbides, which are evenly distributed on the ferrite matrix to form tempered sorbite. Compared with tempering at 250 °C, the carbide phase grows and the ferrite structure decreases slightly.

3.1.3 OM Analysis of the DH1050 Side in HAZ. Figure 12 shows the structure of the HAZ on the DH1050 side of the joint under different tempering treatments, which is mainly composed of a complete quenching zone and an incomplete quenching zone. The peak temperature in the no tempering part of the joint closer to the heat source center (see Fig. 12a) exceeds A_{c3} , and the martensite and ferrite in the original structure are completely austenitized and transformed into plate-like coarse martensite with different orientations and a

small amount of residual austenite after cooling. While the maximum heating temperature in the area far from the weld center (see Fig. 12b) is between A_{c1} and A_{c3} , the martensite and part of ferrite are transformed into austenite, then austenite is transformed into a mixed structure of martensite, ferrite and bainite during cooling. Compared with BM, the number of island martensite in this area decreases obviously, and the retained austenite phase also exists. Due to the recrystallization process, new martensite is formed after cooling. However, part of these martensitic is transformed into ferrite, resulting in softening. This observation is in agreement with the study of Jia (Ref 31), who found that this situation leads to the formation of martensitic and ferrite phases in HAZ. Meanwhile, Gao (Ref 32) found the presence of austenite diffraction peaks in all regions of HAZ, indicating that a small amount of austenite is stored in these regions.

Most of the lath martensite in the complete quenching zone (see Fig. 12c) is decomposed into tempered martensite and

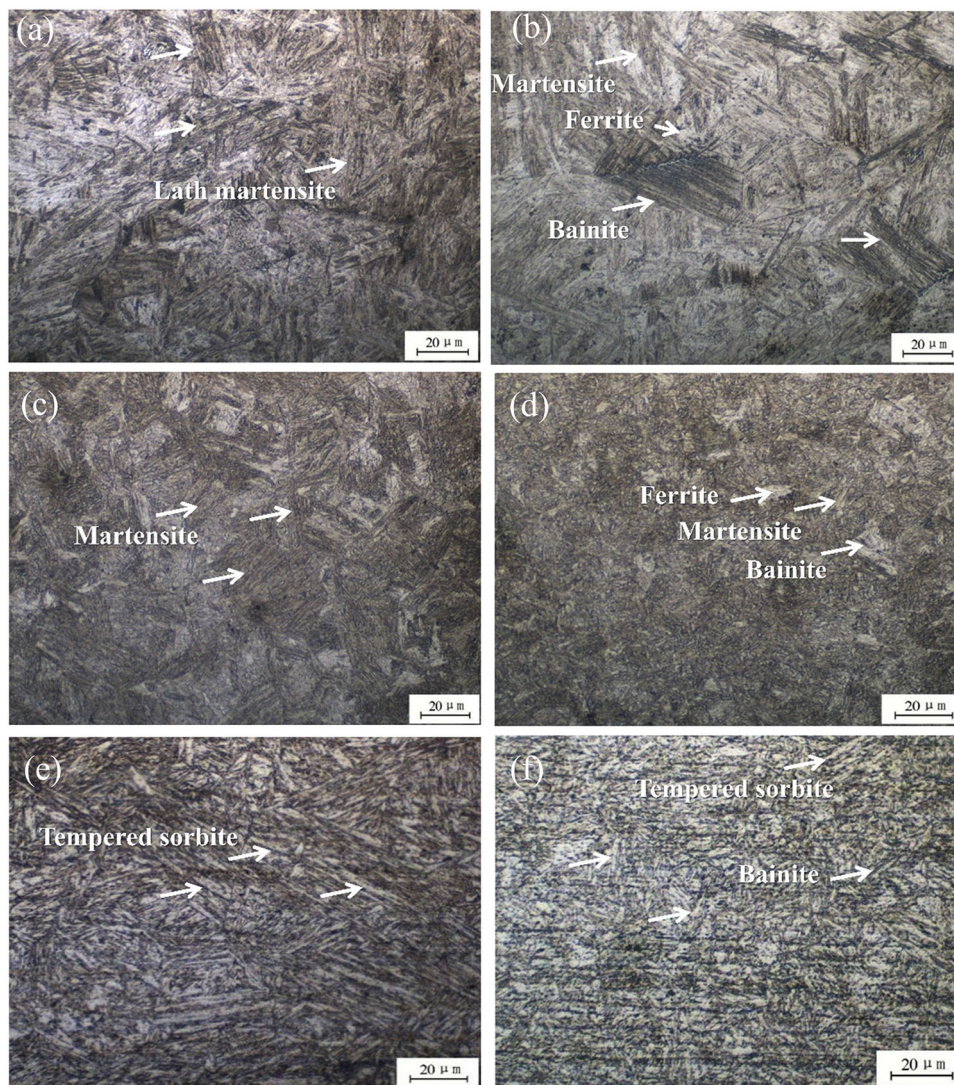


Fig. 12 The microstructure of HAZ on the DH1050 side of the joint under different tempering treatments. (a) Complete quenching zone (no tempering), (b) incomplete quenching zone (no tempering), (c) complete quenching zone (tempering at 250 °C), (d) incomplete quenching zone (tempering at 250 °C), (e) complete quenching zone (tempering at 550 °C), (f) incomplete quenching zone (tempering at 550 °C)

carbide after tempering at 250 °C. The martensite grain is refined and the directionality is weakened. At this time, there is still a small amount of lath martensite in this area, a morphological transformation from lath bundle to lath block. The microstructure of the incomplete quenching zone (see Fig. 12d) is different from that without tempering treatment. The lath martensite is decomposed into tempered martensite, the ferrite phase is increased, the grain becomes fine and the granular carbides were precipitated on the original austenite grain boundary and martensite interface. The upper bainite decomposition disappears and transforms into needle-like bainite.

Compared with the tempering treatment at 250 °C, the tempering treatment at 550 °C resulted in a large amount of decomposition of martensitic in the complete quenching zone (see Fig. 12e). The fine spheroidal carbides are distributed in the ferrite matrix formed by martensite tempering, which is changed into tempered sorbite with certain directivity. A small amount of martensitic structure and preserved austenite could be observed. The amount of ferrite in the incomplete quenching zone (see Fig. 12f) increases, a large amount of martensite structures decomposes, and the structure changes to tempered sorbite. The number of spherical and near spherical carbides increased significantly, evenly distributed on the ferrite matrix, and the grains grew to a certain extent. In addition, a small amount of bainite remains at this time.

3.1.4 SEM and EDS Analysis of the Joint in WZ. Figure 13 shows SEM morphology and EDS analysis of the WZ of the joint before and after tempering treatment. Figure 13(d)-(f) shows the EDS analysis of the A, B, C zones marked in Fig. 13(a)-(c), respectively. The no tempering WZ (see Fig. 13a) has a large amount of plate-like martensite and a small amount of residual austenite. According to the EDS analysis results of zone A (see Fig. 13d and Table 5), the main elements in the lath martensite phase are Al, Si, Mn and Fe. The mass fractions of each element are: Al 1.12, Si 0.66, Mn 2.32 and Fe 95.89 wt.%, respectively.

According to Fig. 13(b), after tempering at 250 °C, martensite in WZ begins to decompose and transform into tempered martensite. The morphology of martensite remains needle-like, and carbides precipitate along the original austenite grain

Table 5 The EDS results in WZ of the welded joint (wt.%)

Location	Elements				
	Fe	Mn	Al	Si	C
A	95.89	2.32	1.12	0.66	...
B	95.73	1.51	0.42	0.40	1.95
C	95.66	2.04	2.30

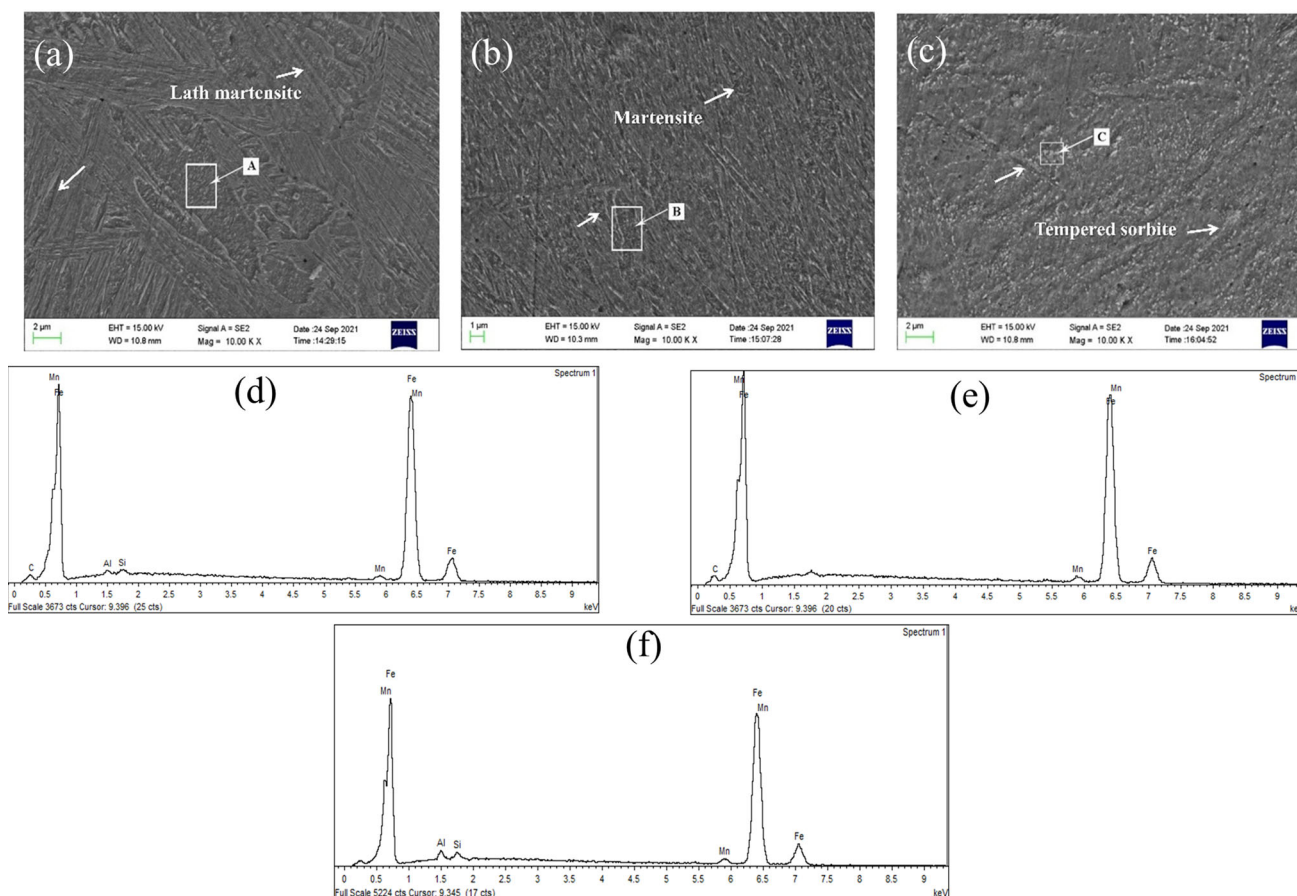


Fig. 13 SEM images and EDS results of the welded joint in WZ under different tempering treatments. (a) No tempering, (b) tempering at 250 °C, (c) tempering at 550 °C, (d) EDS in A zone, (e) EDS in B zone, (f) EDS in C zone

boundary and lath bundle boundary. After low-temperature tempering, the internal atomic activity is improved, and the supersaturated carbon in the martensite starts to precipitate as carbide gradually, which makes the carbon atom content in the surrounding ferrite start to increase. From the EDS analysis results of zone B (see Fig. 13e, Table 5), the main elements of the martensite structure are Al, Si, Mn, Fe and C. The mass fractions of each element are: Al 0.42, Si 0.40, Mn 1.51, Fe 95.73 and C 1.95 wt.%, respectively.

After tempering at 550 °C (see Fig. 13c), the lath martensite structure disappears, the precipitated carbides aggregate and grow into cementite particles, and the mixed structure of fine granular cementite and ferrite is tempered sorbite. After high-temperature tempering, the fine grained carbides are completely precipitated and uniformly distributed on the ferrite matrix (Ref 31). From the EDS analysis results of zone C (see Fig. 13f, Table 5), the main elements of the tempered sorbite structure are Mn, Fe and C. The mass fractions of each element are: Mn 2.04, Fe 95.66 and C 2.30 wt.%, respectively.

3.1.5 SEM Analysis of the CR22MnB5 Side in HAZ. Figure 14 shows the SEM morphology of HAZ on the CR22MnB5 side under different heat treatment processes. The maximum temperature in HAZ of this side near the weld center (see Fig. 14a) exceeds the A_{c3} line. The original structure is completely austenitized and cooled to form lath martensite and a small amount of residual austenite. The maximum heating temperature is between A_{c1} and A_{c3} in the region far away from the heat source. The cooling speed is fast after welding, austenite transforms into lath martensite, ferrite and part of bainite, and ferrite grows up (Ref 15).

The lath martensite decomposes and transforms into tempered martensite after tempering at 250 °C (see Fig. 14b). The cementite is continuously precipitated and the granular cementite is evenly distributed in the two-phase mixture of the ferrite matrix. Part of the retained austenite is decomposed and transformed into lower bainite. However, after the tempering treatment at 550 °C (see Fig. 14c), the ferrite matrix formed during the tempering of martensite is distributed with fine spherical carbides, which transform into tempered sorbite. The number of spherical and subspherical carbides increase significantly and are uniformly distributed on the ferrite matrix, with a certain degree of grain growth. A small amount of slate martensite phase can still be observed at this time.

3.1.6 SEM Analysis of the DH1050 Side in HAZ. SEM morphology of the DH1050 side in HAZ under different heat treatment processes is shown in Fig. 15. The temperature of HAZ near the weld center (see Fig. 15a) is above the A_{c3} line, the original structure is completely austenitized. It is transformed into plate-like martensite and a small amount of residual austenite with different orientation after cooling and the grain size of martensite is coarse. This observation is in agreement with that of Di (Ref 33), who found that the unstable martensitic structures are susceptible to decomposition and austenitic transformation, forming new martensitic structures after cooling, but some unstable martensitic structures is transformed into ferrite.

Lath martensite is decomposed into tempered martensite after tempering at 250 °C (see Fig. 15b). The granular carbide precipitates on the original austenite grain boundary and martensite interface. The formed granular cementite is evenly distributed in the two-phase mixture of ferrite matrix. The upper bainite decomposes and disappears, transforming into needle-like bainite. This observation is in agreement with that of the above OM analysis. After tempering at 550 °C (see Fig. 15c), the martensite phase is decomposed and fine spheroidal carbides are distributed in the ferrite matrix, which is transformed into tempered sorbite. The number of spherical and near spherical carbides increases significantly, evenly distributed in the ferrite matrix. The grains grow up to a certain extent. A few lath martensite and bainite phases can still be observed.

3.2 Mechanical Properties of Joint

3.2.1 Microhardness. The microstructure of the welded joint in each area after different tempering temperature processing will be changed, which will inevitably affect the mechanical properties of the welded joint. The results of microhardness distribution before and after tempering (see Fig. 16) show that the trend of hardness distribution before and after tempering is basically the same, all in WZ at the maximum value of hardness.

The hardness of WZ is higher than that of BM due to the predominantly martensitic structure of the WZ. The hardness has no decrease rapidly at the beginning of the transition from WZ to HAZ, which is related to the fact that the microstructure in the complete quenching zone adjacent to WZ is still mainly composed of martensite. The hardness drops rapidly from HAZ into BM due to the presence of the softening zone, with the lowest hardness being significantly smaller than the average

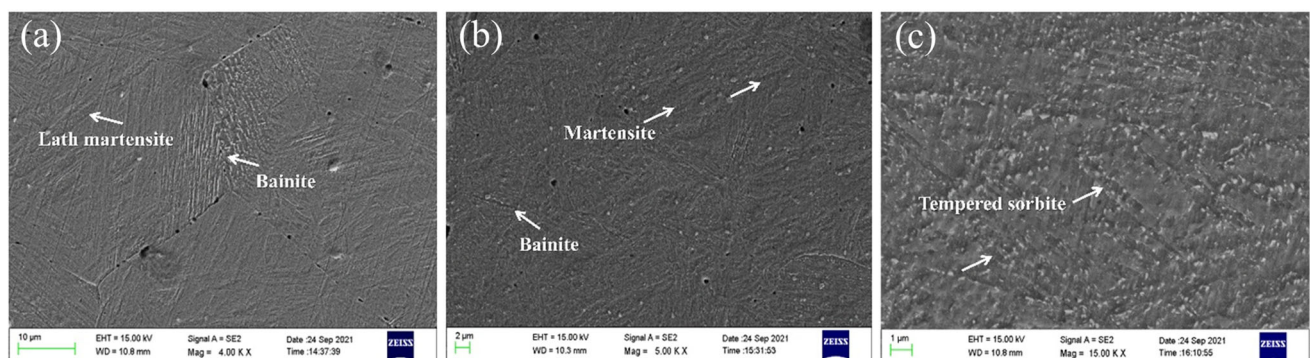


Fig. 14 SEM morphology of HAZ on CR22MnB5 side of the joint under different temper treatments. (a) No tempering, (b) tempering at 250 °C, (c) tempering at 550 °C

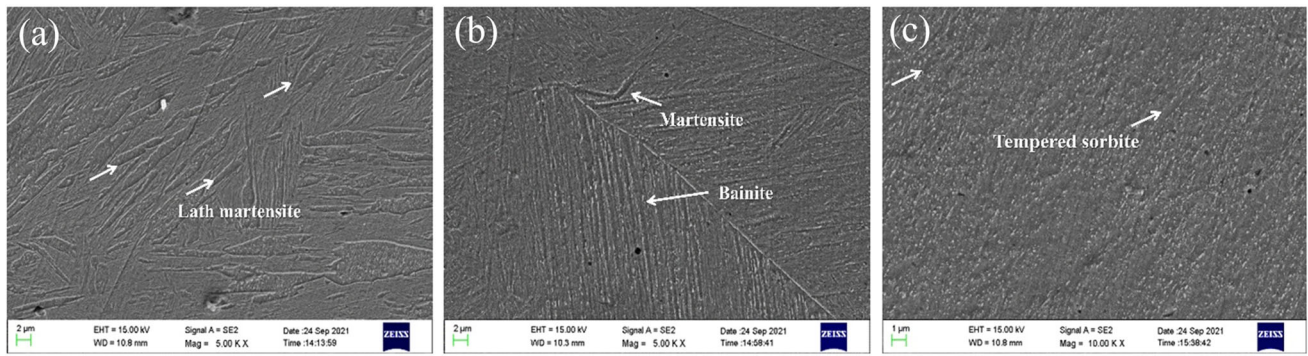


Fig. 15 SEM morphology of HAZ on DH1050 side of the joint under different temper treatments. (a) No tempering, (b) tempering at 250 °C, (c) tempering at 550 °C

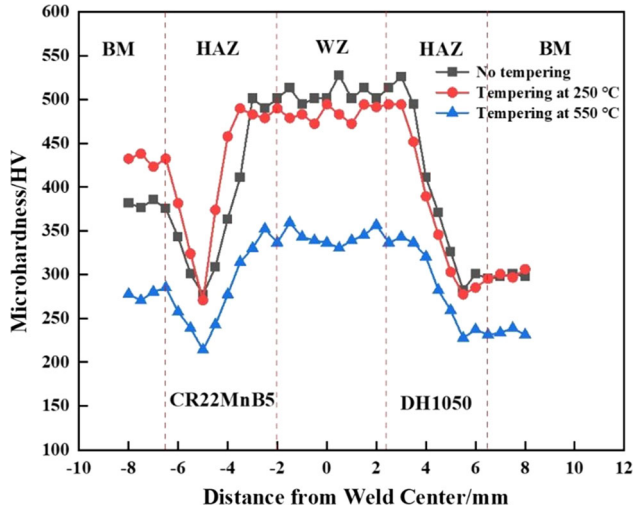


Fig. 16 The microhardness distribution curve of the welded joint

value of BM. It is caused by the fact that the heat in the area far from the heat source center is not enough to transform all the original structure into martensite, but part of the structure into ferrite. The maximum value of hardness before tempering is HV527.5, which is due to the large amount of hard phase, i.e., plate-martensitic structure, produced in WZ after rapid heating and cooling, while the martensitic transformation of HAZ and BM on CR22MnB5 side and DH1050 side is lower than that of WZ due to part of the structure transforms to ferrite (softening zone). The maximum hardness value in WZ of the joint after tempering at 250 °C is HV494.6. The lath martensite in WZ is decomposed to tempered martensite after tempering at 250 °C, while the supersaturated solid solution C is dissolved from α -Fe and formed carbide, which decreased the effect of solid solution strengthening (Ref 33). However, the hardness of WZ decreases significantly after tempering at 550 °C, with a maximum value of HV359.3. Since the higher tempering temperature, the martensitic has been decomposed, and the obvious decomposition products will develop sufficiently (Ref 34). At this time, the martensite is changed into tempered sorbite after tempering, and the solid solution C in α -Fe is further reduced. While the precipitated carbides are heated and grown up, the effect of solid solution strengthening C is greatly weakened and the hardness decreased. The overall hardness distribution of the joint tends to be flat after tempering treatment at 550 °C, with an average value of HV300.4.

The average hardness in BM on the CR22MnB5 side before tempering treatment is HV376.6, while the hardness after tempering at 250 °C is slightly higher with HV432.5 than before. The average hardness in BM decreases significantly with HV 277.9 after tempering at 550 °C compared with that during tempering treatment at 250 °C. The CR22MnB5 side in HAZ has an obvious softening zone. The lowest value of hardness in this zone before tempering is HV277.6, which is basically the same as low-temperature tempering. The lowest value in the softening zone decreased to HV214.2 after high-temperature tempering. The average hardness of BM on the DH1050 side is HV297.8; however, the hardness after tempering at 250 °C is HV294.3. And the average hardness decreased to HV238.9 after tempering at 550 °C. The softening zone also exists in HAZ on the DH1050 side, but the hardness of softening zone has no decrease significantly. The lowest value of hardness in the softening zone of HAZ without tempering treatment is HV282.4, while the trend of hardness distribution after low- and high-temperature tempering is basically the same as that of the CR22MnB5 side. However, the hardness value of softening zone after high-temperature tempering decreases significantly, with the lowest value of HV227.8.

It is found that the change of microstructure after heat treatment has a great influence on the hardness distribution according to hardness test results. The HAZ of the joint is mainly lath martensite before tempering treatment, so the hardness is higher. However, after low-temperature tempering, the lath martensite decomposes into tempered martensite, while the hardness has not decreased significantly. Then, the martensite structure is further transformed after high-temperature tempering, the ferrite content increases, and the microhardness of each zone decreases significantly. This will have a certain impact on the mechanical properties of welded joints. In addition, the HAZ on both sides of the welded joint also has a softening zone, where the hardness of the martensite and ferrite coexistence zone is lower than that of the single lath martensite structure zone.

3.2.2 Tensile Properties. The stress–strain curves of tensile tests for joints under different tempering treatments are shown in Fig. 17. It can be seen that the curves are flat and smooth without an obvious yield deformation process. The tensile strength, yield strength and elongation of the welded joint after different tempering treatments are shown in Table 6. The stress–strain curves of the welded joint without tempering treatment and after tempering at 250 °C are basically the same,

and there is little difference in tensile strength and elongation, which are 890, 883 MPa, 4.85 and 5.12%, respectively. After tempering at 550 °C, the whole joint stress–strain curve is located below the no tempering and cryogenic tempering curves. The tensile strength of the welded joint (724 MPa) is significantly reduced compared with the no tempering joint (890 MPa), but its plastic deformation is increased, with an elongation of 9.65%, which is significantly improved compared to the no tempering joint (4.85%).

In addition, the effect of the tempering on the properties for two base metal is also quite important. Some studies indicated that the tensile strength of the CR22MnB5 side base metal increases initially and then declines as the annealing temperature rises. And the tensile strength is higher after low-temperature tempering at 250 °C than before tempering, while the tensile strength is reduced after high-temperature tempering at 550 °C. Furthermore, after low-temperature tempering, the flexibility and hardness of the CR22MnB5 side base metal have been increased, allowing it to meet service performance (Ref 35, 36). However, there is no information available on the heat treatment properties of the DH1050 steel. Therefore, in this paper, the effect of the tempering on base metal has not been studied, and the further studies on effect on the tempering on properties of base metal are being carried and more details would be reported in the future.

Figure 18 shows the macroscopic morphology of the joint with different tempering treatments after a fracture. All welded joints fractured on the DH1050 side under tensile stress perpendicular to the welding direction. Without tempering treatment and after tempering at 250 °C, the joint fractured in the DH1050 side of HAZ, and the necking occurred. It is a fact

that the tempering softening zone exists on the DH1050 side, where the martensitic structure is thermally decomposed and partially transformed into ferrite, which may lead to a decrease of strength in this region. However, the welded joint fractured on the DH1050 side in BM after tempering at 550 °C, where the obvious necking occurred. The microstructure in this region may lead to the gradual dissolution of the martensite island and the precipitation of carbide after high-temperature tempering, which will reduce the strength of the joint. In addition, the precipitates gradually grow up during high-temperature tempering, which weakens the pinning effect on dislocations. As the carbides are precipitated and aggregated, the ferrite content increases (Ref 37), and the post-fracture elongation of the material increases.

3.2.3 Bending Properties. Figure 19 shows the load–displacement curves of the joint with different tempering curves. In the early stage of load application, the bending load curves of all samples showed a certain linear relationship. When the load reached 300 N, the displacement was 1.6 mm and the load–displacement curve began to bend. For the sample tempered at 550 °C, when the load reached 210 N and the displacement was 1.25 mm, the curve began to bend. Table 7 shows the three-point bending test results of welded joints after different tempering treatments. The maximum bending loads borne without the tempering treatment, after tempering at 250 °C and after tempering at 550 °C are 558, 516 and 438 N, respectively. The maximum bending load of the bent sample decreased by 7.5 and 21.5%, respectively, compared with the sample without tempering treatment after tempering at low and high temperature, while the maximum displacement without tempering, after tempering at 250 °C and after tempering at 550 °C was 6.8, 6.4 and 6.0 mm, respectively. Compared with the no tempering welded joints, using 250 °C tempering and

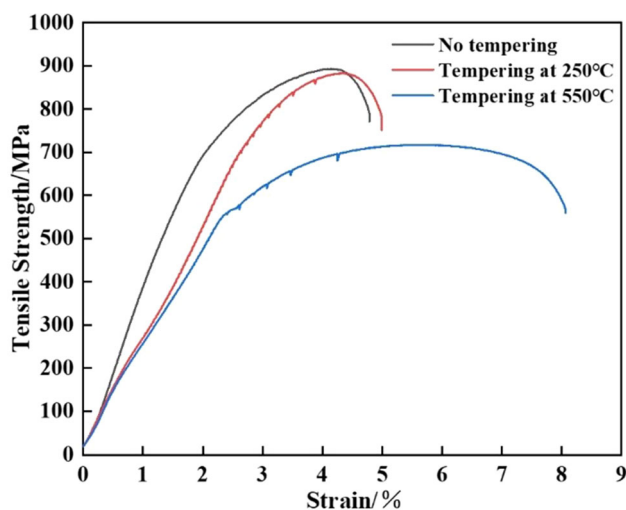


Fig. 17 The stress–strain curves of tensile testing for the welded joint

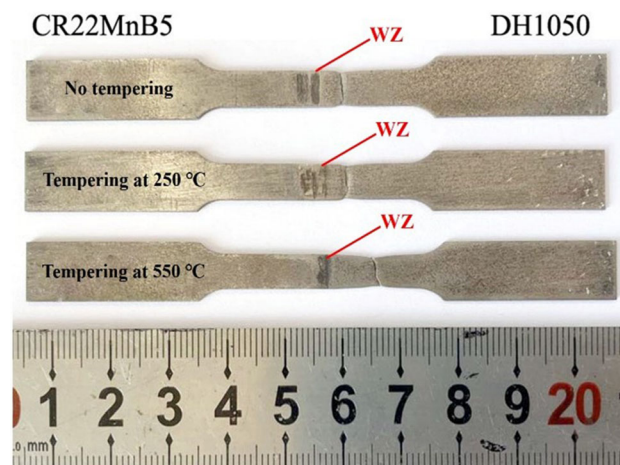


Fig. 18 The tensile fracture characteristics of the welded joints under different tempering treatments

Table 6 The tensile results for the welded joints under different treatments

Process	Tensile strength, Mpa	Yield strength, MPa	Elongation, %
No tempering	890	790	4.85
Tempering at 250 °C	883	782	5.12
Tempering at 550 °C	724	579	9.65

550 °C tempering, the maximum displacement decreased by 5.88 and 11.76%, respectively. Three-point bending testing results show that the welded joints after low-temperature tempering, and the specimen bending resistance does not drop significantly. However, after tempering at 550 °C, the bending resistance of the joint decreased significantly, and the maximum displacement at fracture damage decreased significantly.

Figure 20 shows the standard bending specimens, the bending angle of three-point bending testing. The result indicated that the bending angles of the no tempering, 250 °C tempered and 550 °C tempered specimens are 121, 130 and 137°, respectively (see Fig. 20c). As the tempering temperature

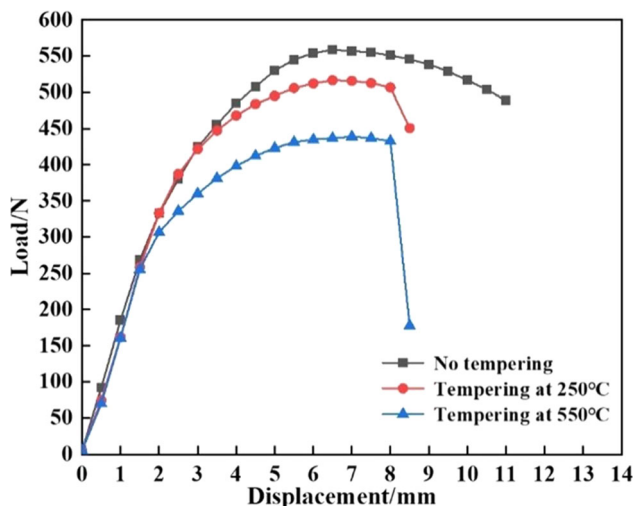


Fig. 19 The bending load displacement curve of the welded joint under different tempering treatments

Table 7 The bending testing results of the welded joints under different treatments

Process	Maximum load, N	Displacement, mm
No tempering	558	6.8
Tempering at 250 °C	516	6.4
Tempering at 550 °C	438	6.0

increases, the bending angle increases dramatically. The smaller the bending angle, the smaller the deformation area. That is, the greater the bending strength, the lower the bending performance of the joint after low- and high-temperature tempering, especially the bending performance of the welded joint after high-temperature tempering.

3.2.4 Electrochemical Corrosion Properties. The polarization curves of the electrochemical test in WZ of welded joints after different tempering treatments are shown in Fig. 21. The corrosion potential and corrosion current density of all samples are shown in Table 8. The corrosion potential of all samples is obviously different in the anodic polarization zone. After different tempering treatments, the corrosion potential of the WZ moves forward, which can effectively improve the corrosion performance of the joint (Ref 38). The corrosion potential of WZ without tempering treatment is -0.728 V. The corrosion potential after tempering at 250 °C is -0.648 V, and that after tempering at 550 °C is -0.688 V. Therefore, the corrosion resistance of WZ after tempering at 250 °C is the best, and that without tempering treatment is the worst.

It is well known that the greater the corrosion current density, the higher the corrosion rate. Therefore, after 250 °C

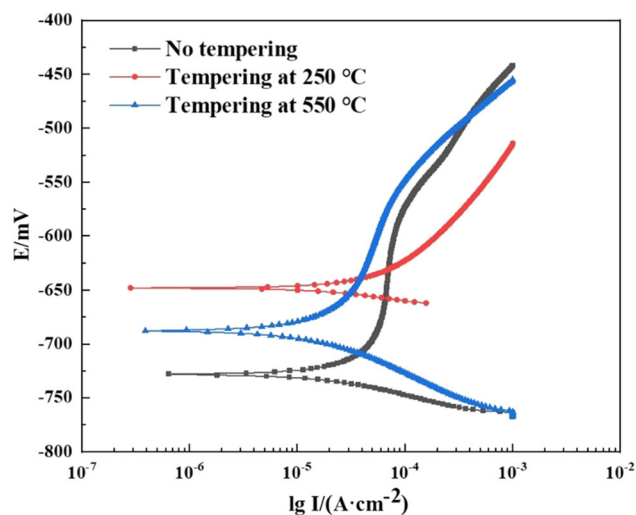


Fig. 21 The polarization curve in WZ of the welded joint under different tempering treatments

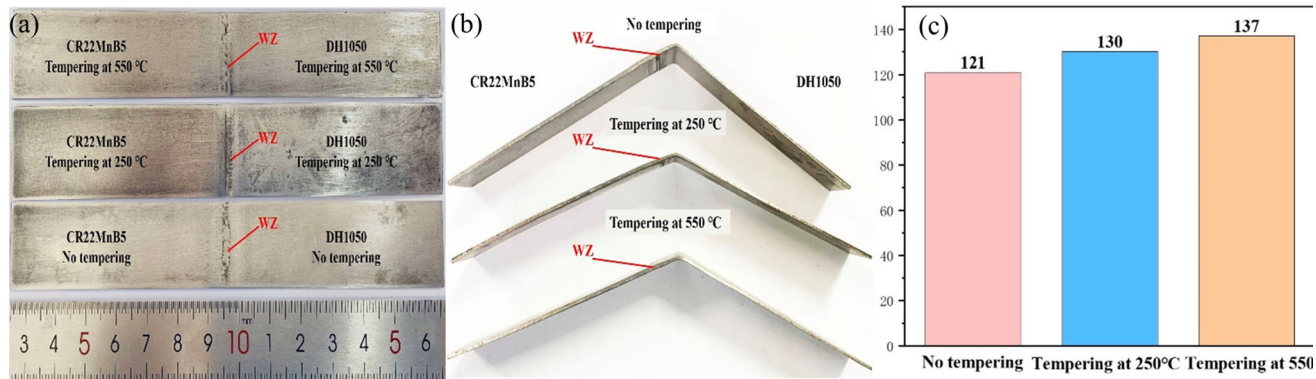


Fig. 20 The images and results of bending testing of the welded joint under different tempering treatments. (a) The standard bending specimen, (b) three-point bending testing results, (c) the images of bending angle results

Table 8 The electrochemical corrosion testing results in WZ under different treatments

Process	Corrosion potential, mV	Corrosion current density, A/cm ²
No tempering	− 728	6.470×10^{-7}
Tempering at 250 °C	− 648	2.844×10^{-7}
Tempering at 550 °C	− 688	3.906×10^{-7}

tempering, the corrosion current density in WZ is the smallest, 2.844×10^{-7} A/cm², indicating that the corrosion rate in WZ under low-temperature tempering is the slowest, and the corrosion resistance is stronger. In addition, since the decomposition of the martensite, precipitation of carbide, increase of ferrite and uneven structure, the corrosion resistance is improved after tempering at 250 °C. However, the maximum corrosion current density in WZ of the joint without tempering treatment is 6.470×10^{-7} A/cm², which indicates that the weld without tempering treatment has the fastest corrosion rate and poor corrosion resistance. At this time, the WZ has coarse lath martensite, and the uneven structure and obvious directionality, so the corrosion performance is poor. By comparing the corrosion current density, it can be concluded that the corrosion resistance from high to low is: tempering at 250 °C > tempering at 550 °C > no tempering.

4. Conclusions

In this paper, the microstructure characteristics, mechanical and electrochemical corrosion properties of unequal thickness CR22MnB5/DH1050 dissimilar high-strength steel welded joint by P-TIG method are studied. When the welding current is 80A and the welding speed is maintained at 3.42 mm/s, the macro-morphology of the joint is optimal. The effect of the post-weld tempering treatment process on the microstructure and properties of dissimilar high-strength steels welded joint is analyzed and discussed. The conclusions are as follows:

- (1) The welded joints are mainly composed of WZ as well as HAZ on both sides. The WZ of the no tempering welded joint is lath martensitic. The HAZ on both sides is further divided into a completely quenching zone and an incompletely quenching zone. The microstructure of the completely quenching zone is mainly lath martensite and a small amount of retained austenite, while the incomplete quenching zone is mainly lath martensite, ferrite and part of the bainite. The higher the tempering temperature, the more sufficient the decomposition of martensite and the growth of decomposition products. The tempering products are the tempered martensite and tempered sorbite, and the solid solution C in α -Fe decreases gradually with the increase of tempering temperature. The number of carbides increases significantly and the grains grow with spherical and subspherical.
- (2) The maximum hardness is obtained in WZ. The HAZ on both sides of the joint has different degrees of softening zone, which the hardness in softening zone of the CR22MnB5 side decreased significantly (about 73.7%

of BM). The lath martensite in WZ decomposes into tempered martensite after tempering at 250 °C, and the supersaturated solid solution C is dissolved from α -Fe and formed carbide. This reduced the effect of solid solution strengthening, and the hardness value decreased slightly. The martensite in WZ is transformed into tempered sorbite, and solid solution C in α -Fe is further reduced after tempering at 550 °C. Since the precipitated carbide is heated and grown up, it greatly weakens the strengthening effect of C solid solution and significantly reduces the hardness.

- (3) The tensile specimens of joints before and after heat treatment are broken on one side of DH1050 steel. The tensile strength and elongation under the no tempering and low-temperature tempering are similar, and they also fractured in the position of the tempering softening zone of HAZ on the DH1050 side. The martensite island in BM gradually dissolves and carbides precipitate after tempering at 550 °C, resulting in the decrease of its tensile strength. The tensile strength (724 MPa) is significantly lower than that of the no tempering joint (890 MPa). However, the elongation of the joint (9.65%) is significantly higher than that of the no tempering joint (4.85%). After tempering at 550 °C, the bending capacity of the specimen decreases obviously, and the bending angle increases gradually with the increase of tempering temperature. When tempering at 250 and 550 °C, the bending angle increases by 7.43 and 13.22%, respectively.
- (4) After different tempering treatments, the electrochemical corrosion potential of WZ moves forward, which can effectively improve the corrosion performance of the joint. The corrosion potential after tempering at 250 °C is − 0.648 V, which is slightly better than that of no tempering (− 0.728 V). It can be concluded that the corrosion resistance from high to low is 250 °C tempering treatment (2.844×10^{-7} A/cm²) > 550 °C tempering treatment (3.90×10^{-7} A/cm²) > no tempering treatment (6.470×10^{-7} A/cm²) by comparing the corrosion current density. The corrosion current density is the minimum after tempering at 250 °C, at which the martensite in the WZ begins to decompose, leading to carbide precipitation and ferrite content increase, which obtains better corrosion resistance.

Acknowledgments

This work was financially supported by the Shandong Provincial Natural Science Foundation, China (Grant No. ZR2016JL017) and the Shandong Provincial Key Research and Development Program, China (Grant No. 2019TSLH0103).

References

1. J. Rissman, C. Bataille, E. Masanet, N. Aden, W.R. Morrow, N. Zhou, N. Elliott, R. Dell, N. Heeren, and H. Brigitta, Technologies and Policies to Decarbonize Global Industry: Review and Assessment of Mitigation Drivers through 2070, *Appl. Energy*, 2020, **266**, p 114848
2. J.M. Allwood, M.F. Ashby, T.G. Gutowski, and E. Worrell, Material Efficiency: Providing Material Services with Less Material Production, *Philos. Trans. R. Soc. A Math. Phys. Eng. Sci.*, 2013, **371**, p 20120496

3. F.N. Bayock, P. Kah, A. Salminen, B. Mvola, and X.C. Yang, Feasibility study of welding dissimilar Advanced and Ultra High Strength Steels, *Rev. Adv. Mater. Sci.*, 2020, **59**, p 54–66
4. T. Mega, K. Hasewak, and H. Kawabe, Ultra High-Strength Steel Sheets for Bodies, Reinforcement Parts, and Seat Frame Parts of Automobile: Ultra High-Strength Steel Sheets Leading to Great Improvement in Crashworthiness, *JFe Technical Report*, 2004, **4**, p 38–43
5. J. Galan, L. Samek, P. Verleysen, K. Verbeken, and Y. Houbaert, Advanced High Strength Steels for Automotive Industry, *Rev. Metal.*, 2012, **48**, p 118–131
6. O. Bouaziz, H. Zurob, and M. Huang, Driving Force and Logic of Development of Advanced High Strength Steels for Automotive Applications, *Steel Res. Int.*, 2013, **84**, p 937–947
7. J.H. Schmitt and T. Iung, New Developments of Advanced High-Strength Steels for Automotive Applications, *C R Phys.*, 2018, **19**, p 641–656
8. M.S. Khan, M.H. Razmpoosh, E. Biro, and Y. Zhou, A Review on the Laser Welding of Coated 22MnB5 Press-Hardened Steel and Its Impact on the Production of Tailor-Welded Blanks, *Sci. Technol. Weld. Joining*, 2020, **25**, p 1–21
9. S.S. Li and H.W. Luo, Medium-Mn Steels for Hot Forming Application in the Automotive Industry, *Int. J. Miner. Metall. Mater.*, 2021, **28**, p 741–753
10. M.D. Taylor, K.S. Choi, X. Sun, D.K. Matlock, C.E. Packard, L. Xu, and F. Barlat, Correlations Between Nanoindentation Hardness and Macroscopic Mechanical Properties in DP980 Steels, *Mater. Sci. Eng., A*, 2014, **597**, p 431–439
11. G. Cheng, F. Zhang, A. Ruimi, D.P. Field, and X. Sun, Quantifying the Effects of Tempering on Individual Phase Properties of DP980 Steel with Nanoindentation, *Mater. Sci. Eng., A*, 2016, **667**, p 240–249
12. R.G. Davies, Influence of Martensite Composition and Content on the Properties of Dual Phase Steels, *Metall. and Mater. Trans. A.*, 1978, **9**, p 671–679
13. H. Wang, L. Liu, H. Wang, and J. Zhou, Control of Defects in the Deep Drawing of Tailor-Welded Blanks for Complex-Shape Automotive Panel, *Int. J. Adv. Manuf. Technol.*, 2022, **119**, p 3235–3245
14. H. Kong, Q. Chao, B. Rolfe, and H. Beladi, One-Step Quenching and Partitioning Treatment of a Tailor Welded Blank of Boron and TRIP Steels for Automotive Applications, *Mater. Des.*, 2019, **174**, p 107799
15. M. Rossini, P.R. Spena, L. Cortese, P. Matteis, and D. Firrao, Investigation on Dissimilar Laser Welding of Advanced High Strength Steel Sheets for the Automotive Industry, *Mater. Sci. Eng., A*, 2015, **628**, p 288–296
16. M.P. Miles, T.W. Nelson, R. Steel, E. Olsen, and M. Gallagher, Effect of Friction Stir Welding Conditions on Properties and Microstructures of High Strength Automotive Steel, *Sci. Technol. Weld. Joining*, 2013, **14**, p 228–232
17. J. Zhang, Q.S. Wu, J.P. Zheng, and Z.J. Huang, Microstructure and Mechanical Properties of Resistance Spot Welded Joint of DP780 Duplex Stainless Steel, *Mater. Mech. Eng.*, 2015, **10**, p 29–31. (Chinese)
18. F. Hayat and B. Sevim, The Effect of Welding Parameters on Fracture Toughness of Resistance Spot-Welded Galvanized DP600 Automotive Steel Sheets, *Int. J. Adv. Manuf. Technol.*, 2012, **58**, p 1043–1050
19. H. Hoffmann, H. So, and H. Steinbeiss, Design of Hot Stamping Tools with Cooling System, *CIRP Ann. Manuf. Technol.*, 2007, **56**, p 269–272
20. N. Farabi, D.L. Chen, J. Li, Y. Zhou, and S.J. Dong, Microstructure and Mechanical Properties of Laser Welded DP600 Steel Joints, *Mater. Sci. Eng., A*, 2010, **527**, p 1215–1222
21. L. Liu, J. Wang, and G. Song, Hybrid Laser-TIG Welding, Laser Beam Welding and Gas Tungsten Arc Welding of AZ31B Magnesium Alloy, *Mater. Sci. Eng., A*, 2004, **381**, p 129–133
22. S.T. Wei, J. Sun, J.W. Liu, and S.P. Lu, Effect of V Content and Tempering Process on Microstructure and Properties of Deposited Metal in TIG Welding of High Strength Steel, *Trans. the China Weld. Instit.*, 2020, **41**, p 1–6. (Chinese)
23. T. Schaupp, D. Schroepfer, A. Kromm, and T. Kannengiesser, Welding Residual Stresses in 960 MPa Grade QT and TMCP High-Strength Steels, *J. Manuf. Process.*, 2017, **27**, p 226–232
24. X.B. Zhang, R. Cao, W. Feng, Y. Peng, J. Fen, and J.H. Chen, Fracture Mechanism of In-Situ Tensile of TIG Welding Joints for 980MPa High Strength Steel, *China Mech. Eng.*, 2010, **21**, p 2746–2750. (Chinese)
25. H.J. Zhang, G.J. Zhang, J.H. Wang, and L. Wu, Effect of Thermal Cycle of Double Side Double Gas Arc Welding on Microstructure and Properties of Low Alloy High Strength Steel, *Trans. China Weld. Instit.*, 2007, **10**, p 81–84. (Chinese)
26. E. Kalácska, K. Májlinger, E.R. Fábrián, and P.R. Spena, MIG-Welding of Dissimilar Advanced High Strength Steel Sheets, *Mater. Sci. Forum*, 2017, **885**, p 80–85
27. J. Jia, S.L. Yang, W.Y. Ni, J.Y. Bai, and Y.S.L. Lin, Microstructure and Properties of Fiber Laser Welded Joints of Ultrahigh-strength Steel 22MnB5 and its Dissimilar Combination with Q235 Steel, *ISIJ Int.*, 2014, **54**, p 2881–2889
28. F. Li, M. Fu, and J. Lin, Effect of Cooling Path on Phase Transformation of Boron Steel, *Proced. Eng.*, 2014, **81**, p 1707–1712
29. K.I. Yaakob, M. Ishak, S. Idris, M.H. Aiman, and M.M. Quazi, Characterization of Heat-Treated Gas Metal Arc-Welded Boron Steel Sheets, *Int. J. Adv. Manuf. Technol.*, 2018, **94**, p 827–834
30. S. Son, Y.H. Lee, D.W. Choi, K.R. Cho, S.M. Shin, Y. Lee, S.H. Kang, and Z. Lee, Investigation of the Microstructure of Laser-Arc Hybrid Welded Boron Steel, *JOM*, 2018, **70**, p 1548–1553
31. J. Jia, S.L. Yang, W.Y. Ni, and J.Y. Bai, Microstructure and Mechanical Properties of Fiber Laser Welded Joints of Ultrahigh-Strength Steel 22MnB5 and Dual-Phase Steels, *J. Mater. Res.*, 2014, **29**, p 2565–2575
32. S. Gao, Y. Li, L. Yang, and W. Qiu, Microstructure and Mechanical Properties of Laser-Welded Dissimilar DP780 and DP980 High-Strength Steel Joints, *Mater. Sci. Eng., A*, 2018, **720**, p 117–129
33. H. Di, Q. Sun, X. Wang, and J. Li, Microstructure and Properties in Dissimilar/Similar Weld Joints Between DP780 and DP980 Steels Processed by Fiber Laser Welding, *J. Mater. Sci. Technol.*, 2017, **33**, p 1561–1571
34. H. Zhao, R. Huang, Y. Sun, C. Tan, and G. Li, Microstructure and Mechanical Properties of Fiber Laser Welded QP980/Press-Hardened 22MnB5 Steel Joint, *J. Market. Res.*, 2020, **9**, p 10079–10090
35. O. Çavuşoğlu, O. Çavuşoğlu, A.G. Yılmazoğlu, U. Üzel, H. Aydın, and A. Güral, Microstructural Features and Mechanical Properties of 22MnB5 Hot Stamping Steel in Different Heat Treatment Conditions, *J. Market. Res.*, 2020, **9**, p 10901–10908
36. J. Jeong, S.C. Park, G.Y. Shin, C.W. Lee, T.J. Kim, and M.S. Choi, Effects of Tempering Condition on the Microstructure and Mechanical Properties of 30MnB5 Hot-Stamping steel, *Korean J. Metals Mater.*, 2018, **56**, p 787–795
37. Z.J. Zhai, Y. Cao, L. Zhao, Y. Peng, Z.L. Tian, and J. Zhu, Effect of Heat Input on Microstructure and Mechanical Properties of DP980 Laser Welded Steel, *J. Iron Steel Res.*, 2020, **32**, p 66–73. (Chinese)
38. Z. Zhou, W.J. Zheng, D. Feng, T. Xu, and J. Yang, Mechanical Properties and Corrosion Resistance of Cold Metal Transfer Small-Bore Thin-Walled Tube Butt Welded Joints of UNS S32205 Duplex Stainless Steel, *J. Mater. Eng. Perform.*, 2022, **31**, p 4531–4544

Publisher's Note Springer Nature remains neutral with regard to jurisdictional claims in published maps and institutional affiliations.

Springer Nature or its licensor (e.g. a society or other partner) holds exclusive rights to this article under a publishing agreement with the author(s) or other rightsholder(s); author self-archiving of the accepted manuscript version of this article is solely governed by the terms of such publishing agreement and applicable law.